Metal–Organic Frameworks Hot Paper

International Edition: DOI: 10.1002/anie.201808716
German Edition: DOI: 10.1002/ange.201808716

Molecular Sieving of Ethane from Ethylene through the Molecular Cross-Section Size Differentiation in Gallate-based Metal–Organic Frameworks

Zongbi Bao, Jiawei Wang, Zhiguo Zhang, Huabin Xing, Qiwei Yang, Yiwen Yang, Hui Wu, Rajamani Krishna, Wei Zhou, Banglin Chen,* and Qilong Ren**

Abstract: *Purification of C_2H_4 from an C_2H_4/C_2H_6 mixture, one of the most important while challenging industrial separation processes, is mainly through energy-intensive cryogenic distillation. Now a family of gallate-based metal–organic framework (MOF) materials is presented, M-gallate (M = Ni, Mg, Co), featuring 3D interconnected zigzag channels, the aperture sizes of which (3.47–3.69 Å) are ideally suitable for molecular sieving of ethylene (3.28 × 4.18 × 4.84 Å^3) and ethane (3.81 × 4.08 × 4.82 Å^3) through molecular cross-section size differentiation. Co-gallate shows an unprecedented IAST selectivity of 52 for C_2H_4 over C_2H_6 with a C_2H_4 uptake of 3.37 mmol g^{-1} at 298 K and 1 bar, outperforming the state-of-the-art MOF material NOTT-300. Direct breakthrough experiments with equimolar C_2H_4/C_2H_6 mixtures confirmed that M-gallate is highly selective for ethylene. The adsorption structure and mechanism of ethylene in the M-gallate was further studied through neutron diffraction experiments.*

Olefin/paraffin separations are industrially critical processes, providing various primary feedstocks for the industrial manufacture of a variety of products, particularly household plastics.[1] Their separations have been recognized as one of the seven chemical separations to change the world because the total energy used for ethylene and propylene separation alone accounts for more than 0.3% of the global energy consumption.[2] Due to the similar sizes and volatilities of the molecules, industrial separation of ethylene from ethane currently relies on energy-intensive cryogenic distillation at high pressures (up to 22 bar) and temperatures as low as −25 °C.[3] Tremendous energies could be saved if materials enabling the efficient separation of ethylene/ethane at ambient temperature and pressure were developed.

For this purpose, tremendous efforts have been devoted to investigate a great number of separation agents, such as membranes,[4] organic solvent-based absorbents,[5] and porous solid adsorbents.[6] Principally, adsorptive separation based on porous solid materials is a prospective and economically viable alternative to the energy-intensive distillation process. To develop adsorbents which preferentially adsorb ethane is of a practically significant interest for the separation of ethylene/ethane mixture, but the adsorption selectivity ever reported for ethane over ethylene is still not high enough.[7] Nowadays, one of the most popular adsorption-based separations of ethane and ethylene in porous materials was based on selective π-complexation interaction between ethylene and transition metals such as Ag^+/Cu^+ ions supported on alumina, resins, and zeolites.[8] However, ethylene is strongly bound and difficult to recover from these composite adsorbents. The complexation with metals may also lead to highly unstable and explosive products. Besides, some metal–organic frameworks (MOFs) with open metal sites (OMSs) rendered similar π-complexation towards ethylene molecules.[9] For instance, the series of MMOF-74 (M = Mg, Co, Ni, Mn, Fe) materials are an archetypal example with high-density OMSs, and perform well for the ethylene/ethane separation owing to a side-on coordination of the carbon–carbon double bond to the metal centers.[10] However, simultaneous co-adsorption of ethane resulted from polarization of OMSs in MMOF-74 is unavoidable, making it difficult to obtain high-purity ethylene at low cost of regeneration energy.

Ideal porous materials for gas separation are those with suitable pore sizes and geometries for size or shape sieving, only taking up smaller molecules while blocking the larger ones. Fortunately, ultra-fine tuning of the topology of the aperture could be readily accomplished in MOFs via ligand and/or metal ion substitutions,[11] as well in some zeolites.[6,8b,12] Benefitting from their highly ordered and well-defined pore structures, and adjustable pore dimensions, MOFs have attracted considerable attention as porous solid adsorbents in the field of gas storage and separation during the last two decades.[13] Among some of the pioneering works, molecular exclusion of methane and nitrogen from carbon

[*] Dr. Z. B. Bao, Dr. J. W. Wang, Prof. Z. G. Zhang, Prof. H. B. Xing, Dr. Q. W. Yang, Prof. Y. W. Yang, Prof. Q. L. Ren
Key Laboratory of Biomass Chemical Engineering of Ministry of Education, College of Chemical and Biological Engineering
Zhejiang University
Hangzhou 310027 (P. R. China)
E-mail: renql@zju.edu.cn

Prof. B. L. Chen
Department Department of Chemistry
University of Texas at San Antonio
One UTSA Circle, San Antonio, TX 78249-0698 (USA)
E-mail: banglin.chen@utsa.edu

Dr. H. Wu, Prof. W. Zhou
NIST Center for Neutron Research
National Institute of Standards and Technology
Gaithersburg, MD 20899-6102 (USA)
E-mail: wzhou@nist.gov

Prof. R. Krishna
Van't Hoff Institute for Molecular Sciences, University of Amsterdam
Science Park 904, 1098 XH Amsterdam (The Netherlands)

Supporting information and the ORCID identification number(s) for the author(s) of this article can be found under: https://doi.org/10.1002/anie.201808716.

dioxide,[14] ethylene, and carbon dioxide from acetylene,[15] propane from propylene,[16] branched paraffins from normal paraffins[17] have been successfully achieved by fine tuning of the MOF structures. However, it remains an ongoing challenge to seek out a porous solid material with suitable pore size and window shape to achieve the molecular sieving of ethylene and ethane with high enough efficiency.[8b]

Previously, the studies aimed at molecular sieving mainly focused on the difference between the kinetic diameters of gas adsorbates and the pore size of the adsorbent, and few insights into the complete molecular sieving through their van der Waals molecular dimension differentiation were obtained. Herein, we reported a family of MOF materials whose pore windows are ideally suitable for molecular sieving of ethylene and ethane through molecular cross-section size differentiation. The gallate-based MOFs feature three-dimensionally interconnected zigzag channels (3.47×4.85, 3.56×4.84, 3.69×4.95 Å^2 for Ni, Mg, Co-gallate, respectively). From the kinetic diameter point of view, it seems impossible for both ethylene (with the kinetic diameter of 4.163 Å) and ethane (4.443 Å) to get into the pore channels.[18] On the contrary, the appropriate aperture size is theoretically perfect for the separation of ethane ($3.81\times4.08\times4.82$ Å^3) and ethylene ($3.28\times4.18\times4.84$ Å^3)[19] (Supporting Information, Figure S1) considering that the aperture size is slightly larger than the minimum cross-section size of ethylene molecule (3.28×4.18 Å^2) but obviously smaller than that of ethane (3.81×4.08 Å^2; Figure 1c; Supporting Information, Figure S2). This means that ethane molecules could be excluded from the pore channels while ethylene molecules could enter the pore. Our hypothesis was indeed verified by adsorption isotherms and breakthrough experiments on M-gallate. The adsorption structure and mechanism of ethylene in the zigzag channels was further studied through neutron diffraction experiments. Our results show that M-gallate is a new benchmark porous material for adsorptive separation of ethylene and ethane.

The gallate-based MOFs, M-gallate ($M(C_7O_5H_4)\cdot2H_2O$, M = Ni, Mg, Co), were prepared from the reaction of gallic acid and metal salts. The crystal structure of Ni-gallate was resolved by single-crystal X-ray diffraction analysis, and the structure of Mg, Co-gallate were inferred from the powder X-ray diffraction data thanks to the excellent crystallinity. Structure resolution revealed that the as-synthesized M-gallate are isostructural and crystallized in the $P3_221$ space group (Supporting Information, Table S1), in agreement with the previous report.[20] The framework structure is composed of infinite chains of corner-sharing distorted MO_6 octahedra connected through the organic ligands (four O atoms from the phenolic hydroxy groups of two different ligands, and two O from the carboxyl groups of another two ligands). The regular main channels are formed by spiral extension of the connection of metal octahedra and organic ligands around the *c* axis, along with regular branched channels leaning against the main ones (Figure 1a,b). Moreover, M-gallate shows the ideal quasi-discrete fusiform branched channels as

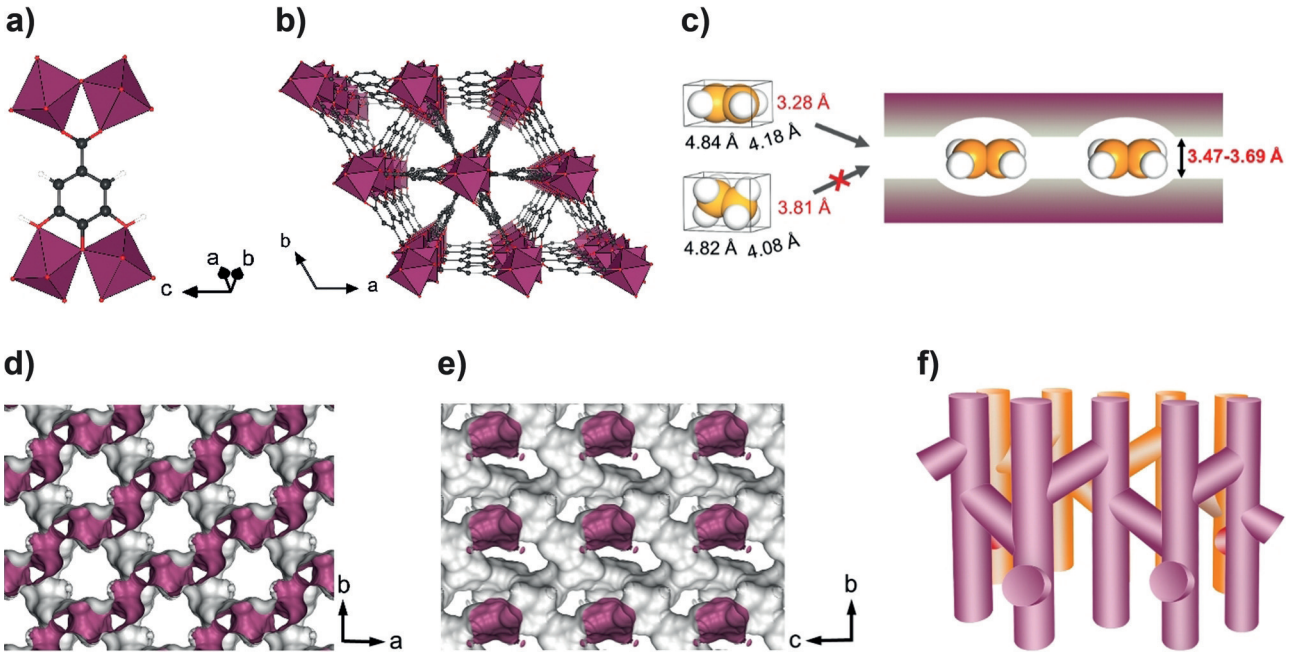

Figure 1. a) The coordination environment of gallate ligand and MO_6. M purple, C black, O red, H white. b) Perspective view of the structure along the *c* axis showing the triangular main channels and the regular branched channels leaning against the main ones. The H atoms are omitted for clarity. c) Diagram of the fusiform branched channels. Only ethylene can favorably enter the cavity because the limiting aperture size of M-gallate (3.47×4.85 Å^2 for Ni-gallate, 3.56×4.84 Å^2 for Mg-gallate, and 3.69×4.95 Å^2 for Co-gallate) matches well with the smallest cross-section size of C_2H_4 (3.28×4.18 Å^2), but is smaller than that of C_2H_6 (3.81×4.08 Å^2). The C atoms in C_2H_4 and C_2H_6 are particularly presented in orange. d),e) Accessible Connolly surface calculated with a Connolly radius of 1.0 Å. The quasi-discrete cavities of the fusiform branched channels are restrained by the narrow pore windows. f) Diagram of the zigzag channels. The zigzag channels in different layers are colored by purple and orange, respectively.

molecular sieves, where the larger cavities are interconnected by very narrow windows (Figure 1 d,e; Supporting Information, Figure S2). The interlaced zigzag channels are fully empty after the guest molecule removed (Figure 1 f), and the crystal lattice of M-gallate becomes slightly distorted with symmetry changing from the $P3_221$ to $P3_1$ space group (Supporting Information, Figure S3 and Table S2). The pore size still matches well with the smallest cross-section size of ethylene and remains smaller than that of ethane.

The permanent porosity of M-gallate was confirmed by adsorption isotherms of CO_2 at 195 K (Supporting Information, Figure S4) with Brunauer–Emmett–Teller (BET) surface areas estimated to be 424, 559, and 475 $m^2 g^{-1}$ for Ni, Mg, Co-gallate, respectively. Based on the encouraging microporous porosity characteristics, the separation potential for C_2H_4/C_2H_6 mixture was first examined by single-component equilibrium adsorption isotherms. As shown in Figure 2 a and the Supporting Information, Figures S5–S7, satisfactory C_2H_4 adsorption capacity is achieved on all M-gallates. Specially, Co-gallate exhibits the highest C_2H_4 uptake of 3.37 mmol g^{-1} at 298 K and 1 bar. As a very important parameter in industrial adsorptive separation process, the volumetric uptake of C_2H_4 on Co-gallate reaches up to 5.18 mmol mL^{-1}, surpassing most state-of-the-art performers, including the benchmark MOF material NOTT-300 (4.90 mmol mL^{-1}), next only to the family of MMOF-74 (Figure 2 c; Supporting Information, Table S3). It implies the high productivity of ethylene in the industrial adsorption process. It is worth noting that all M-gallate are capable of preventing C_2H_6 from entering the channels as evident with a low uptake (less than 0.31 mmol g^{-1}) at 298 K up to 1 bar. It is dramatically lower than those of best-performing porous materials, including zeolite 13X, NOTT-300 and the family of MOF-74 (Supporting Information, Table S3). Therefore, our adsorption findings confirmed that M-gallate is capable of efficiently blocking the slightly larger ethane molecules on the premise of high ethylene uptake.

In light of molecular exclusion of ethane, M-gallate show remarkable ideal adsorbed solution theory (IAST) selectivity for the equimolar C_2H_4/C_2H_6 mixture (Figure 2 b). Particularly, Co-gallate exhibits an unprecedented adsorption selectivity of 52 at 298 K and 1 bar, outperforming all MOF-based adsorbents ever reported, and setting up a new benchmark for the C_2H_4/C_2H_6 separation (Figure 2 b,c). To further confirm such outstanding separation performance of M-gallate for ethylene/ethane mixture, we also investigated the experimental breakthrough tests for C_2H_4/C_2H_6 (50/50, *v/v*) mixture. Figure 2 d shows the dimensionless concentration of C_2H_4/C_2H_6 exiting the adsorber packed with M-gallate as a function of the time at 1 bar. Complete separation was realized by all M-gallate, whereby C_2H_6 broke through very soon because of low uptake capacity; nevertheless, the signal of C_2H_4 was not detected longer than 55 min, denoting that pure C_2H_6 could be obtained until C_2H_4 was eluted. On the other hand, the bound C_2H_4 molecules in the column can be easily desorbed by an inert gas (helium) purge or the vacuum swing method after adsorption saturation to obtain high-purity C_2H_4 due to relatively weak interaction between C_2H_4 and M-gallate. As an important parameter to evaluate the strength of interaction between the adsorbent and the adsorbate, the isosteric heat of adsorption (Q_{st}) of C_2H_4 was calculated using the Clausius–Clapeyron equation. The obtained Q_{st} value at zero-coverage was 32, 39, 44 kJ mol^{-1} for Ni, Mg, Co-gallate (Supporting Information, Figure S8 and Table S3), which is remarkably lower than those of π-complexation-based MOF-74 with open

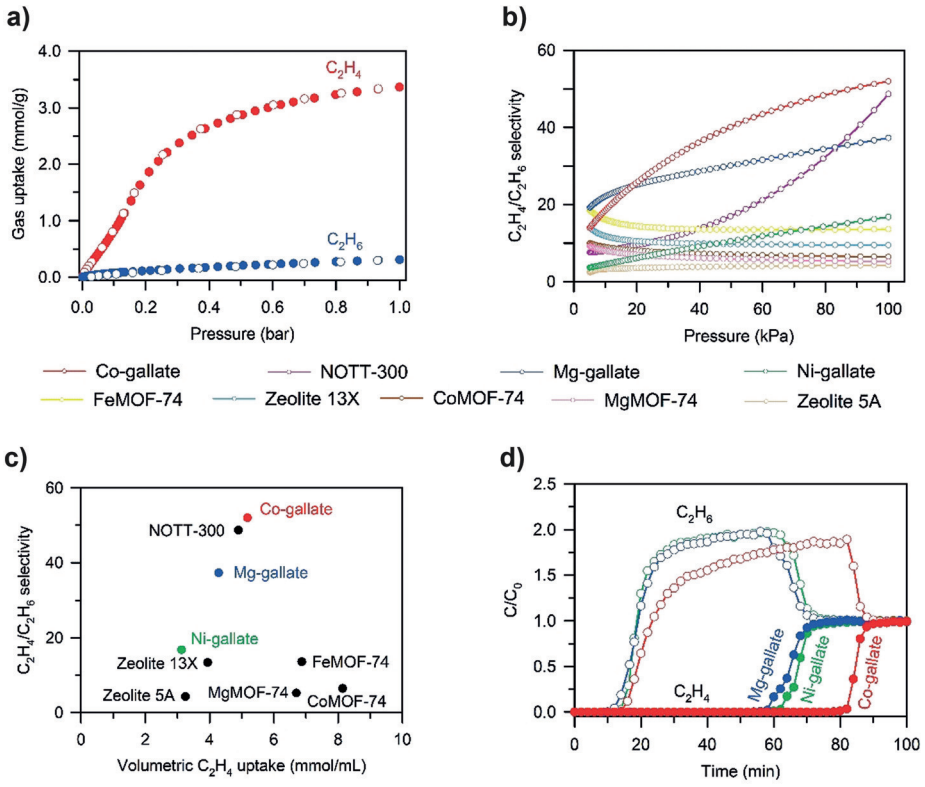

Figure 2. a) Single-component adsorption isotherms of C_2H_4 (red) and C_2H_6 (blue) in Co-gallate at 298 K in the pressure range of 0–1 bar. Empty symbols represent desorption data. b) Comparison of IAST selectivities for equimolar C_2H_4/C_2H_6 mixtures in M-gallate with other best-performing materials in the range of 0–1 bar. The adsorption isotherms were collected at 318 K for FeMOF-74,[10a] 298 K for M-gallate, MgMOF-74[9a] and zeolite 13X,[21] 296 K for CoMOF-74,[22] 293 K for NOTT-300,[23] and 283 K for zeolite 5A.[24] c) Comparison of C_2H_4/C_2H_6 adsorption selectivity and volumetric C_2H_4 uptake at 1 bar in M-gallate and other best-performing materials. d) Experimental breakthrough curves of M-gallate for the equimolar C_2H_4/C_2H_6 mixture at 273 K and 1 bar with a constant flow rate of 0.5 mL min^{-1}.

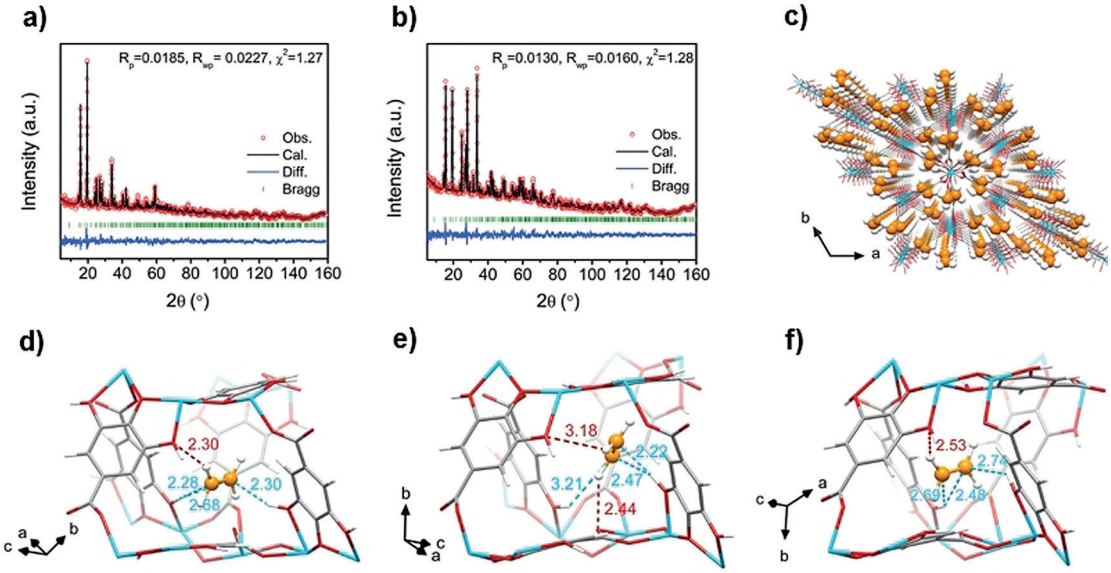

Figure 3. a),b) Rietveld refinements of the NPD data for a) bare Mg-gallate and b) C_2D_4-loaded Mg-gallate, both measured at 200 K. The ligand molecules and the C_2D_4 molecules were kept as rigid bodies during the refinement. Experimental (circles), calculated (line), and difference (line below observed and calculated) neutron powder diffraction profiles are shown. Vertical bars indicate the calculated positions of Bragg peaks. The goodness of fit data are shown in insets. c) Neutron diffraction crystal structure of Mg-gallate·0.485 C_2D_4 at 200 K from Rietveld analysis showing all C_2D_4 molecules are located in the branched channels. d)–f) Adsorption binding sites in Mg-gallate. d) Site I, e) Site II, and f) Site III. The C···H supramolecular interactions of C···H—O and C—D···O hydrogen-bonds are highlighted in cyan and red, respectively. Mg, C, O, H in Mg-gallate are represented by cyan, gray, red, and white, respectively; C and D in C_2D_4 are represented by orange and white, respectively.

metal sites (Supporting Information, Table S3) despite higher than NOTT-300 (16 kJ mol^{-1}). These adsorption results suggest M-gallate is a promising candidate for C_2H_4/C_2H_6 separation. To further understand the outstanding separation performance of M-gallate, the adsorption structure of C_2D_4 in Mg-gallate was established through high-resolution neutron powder diffraction (NPD) experiments (Figure 3a,b). As shown in Figure 3c and the Supporting Information, Figure S9, different from the water molecules residing in the *c*-axis straight channels (Supporting Information, Figure S10), all C_2D_4 molecules are located preferentially at the intersections of the straight and zigzag channels, most probably attributed to the larger molecule dimensions of C_2D_4 than H_2O, as well as the smaller aperture size of *c*-axis straight channels for hosting. Due to the slightly distorted trigonal lattice of activated Mg-gallate, the adsorbed C_2D_4 molecules belong to three crystallography sites, which differ only a little in terms of local pore environment (Figure 3d-f; Supporting Information, Figure S11). Taking Site I (Figure 3d) as an example, the C_2D_4 molecule is surrounded by a cycle composed of metal ions and two neighboring gallate ligands, and bound to the framework through cooperative supramolecular interactions between C(δ^-) of C_2D_4 and H(δ^+) from −OH of the two parallel gallate ligands (C···H—O = 2.28–2.68 Å). Furthermore, the side-on C—D···O hydrogen bonding interactions between C—D of C_2D_4 and the gallate ligand further strengthened the restraint against the C_2D_4 molecules. The bond length of the supramolecular interactions and hydrogen bonds had a similar but a very slight change at Site II and III (Figure 3e,f) attributed to the slight distortion of the framework structure after dehydration (Supporting Information, Figure S3).

Among M-gallate, Mg-gallate not only keeps intermediate C_2H_4/C_2H_6 separation performance between Co- and Ni-gallate, but also is more thermally stable than Ni, Co-gallate, as evident by the TGA results (Supporting Information, Figure S12), arising from the higher hardness of Mg^{II}. Moreover, Mg^{II} salt is also cheaper and comparatively nontoxic compared with most transition metals.[25] Hence, we chose Mg-gallate to further investigate the industrial potential. Mg-gallate could be readily synthesized from gallic acid (ca. \$10 kg^{-1}), which is produced on a massive scale from biomass, and the whole synthetic process is environmentally friendly without the use of organic solvents. Furthermore, the PXRD patterns and C_2H_4 uptake of Mg-gallate are still consistent with that of the as-synthesized sample even after being exposed in humid atmosphere (20 °C, and 75 % humidity) for 3 weeks (Supporting Information, Figures S13, S14), proving that Mg-gallate is highly stable against water vapor. Subsequently, multiple breakthrough tests revealed that Mg-gallate maintained its C_2H_4 uptake and complete molecular exclusion of C_2H_6 over 10 cycles (Supporting Information, Figure S15), illustrating the recyclability of Mg-gallate in the separation of the C_2H_4/C_2H_6 mixture. Besides, the excellent chemical and water stability of Mg-gallate was verified by unchanged PXRD patterns even after soaking in water and ethanol for 5 weeks (Supporting Information, Figure S16). Moreover, we investigated the feasibility of usage of Mg-gallate in industrial practice, and powder Mg-gallate was obtained by scale-up synthesis in the flask at ambient pressure. The PXRD patterns (Supporting Information, Figure S13) and adsorption isotherm for C_2H_4 (Supporting Information, Figure S17) exhibit no notable differences, indicating that the performance of efficient separation for

gas mixture would not differ from each other. Afterwards, millimeter-sized extrudates were shaped by addition of a binder material (Supporting Information, Figure S18), and the excellent separation performance for C_2H_4/C_2H_6 mixture was well retained (Supporting Information, Figures S19, S20). Therefore, Mg-gallate shows great potential in the practical separation of C_2H_4 and C_2H_6 in view of ready availability of ligand and easy preparation.

In summary, we demonstrated for the first time that a family of M-gallate (M = Ni, Mg, Co) MOFs are capable of selectively adsorbing ethylene while blocking ethane because of the perfect aperture dimension falling in the range between the minimum cross-section size of ethylene and that of ethane, affording benchmark high selectivity of ethylene over ethane. High ethylene uptake may also be realized due to high utilization efficiency of the quasi-discrete branched channels, where cooperative supramolecular interactions between ethylene and framework occurred. With several merits including readily available ligand, high stability against water vapor combined with the excellent maintenance of separation performance, M-gallate shows great potential in industrial practice, such as the pressure-swing adsorption process.

Acknowledgements

This work is supported by Zhejiang Provincial Natural Science Foundation of China (No.LR17B060001), National Natural Science Foundation of China (No.21722609 and No.21436010), and National Key R&D Program of China (No. 2016YFB0301500), and partly supported by Welch Foundation (AX-1730). We thank Danyan Xie and Yingcai Zhao at Zhejiang University for their help in adsorption isotherm measurements.

Conflict of interest

The authors declare no conflict of interest.

Keywords: adsorption separation · ethane · ethylene · metal–organic frameworks · purification

How to cite: *Angew. Chem. Int. Ed.* **2018**, *57*, 16020–16025
Angew. Chem. **2018**, *130*, 16252–16257

[1] a) R. B. Eldridge, *Ind. Eng. Chem. Res.* **1993**, *32*, 2208–2212; b) H. A. Wittcoff, B. G. Reuben, J. S. Plotkin, *Industrial organic chemicals*, Wiley, Hoboken, **2005**.
[2] D. S. Sholl, R. P. Lively, *Nature* **2016**, *532*, 435–437.
[3] R. T. Yang, *Adsorbents: fundamentals and applications*, Wiley, Hoboken, **2003**.
[4] K. Tanaka, A. Taguchi, J. Hao, H. Kita, K. Okamoto, *J. Membr. Sci.* **1996**, *121*, 197–207.
[5] T. A. Reine, R. B. Eldridge, *Ind. Eng. Chem. Res.* **2005**, *44*, 7505–7510.
[6] P. J. Bereciartua, Á. Cantín, A. Corma, J. L. Jordá, M. Palomino, F. Rey, S. Valencia, E. W. Corcoran, P. Kortunov, P. I. Ravikovitch, A. Burton, C. Yoon, Y. Wang, C. Paur, J. Guzman, A. R. Bishop, G. L. Casty, *Science* **2017**, *358*, 1068–1071.
[7] a) C. Gücüyener, J. van den Bergh, J. Gascon, F. Kapteijn, *J. Am. Chem. Soc.* **2010**, *132*, 17704–17706; b) J. Pires, M. L. Pinto, V. K. Saini, *ACS Appl. Mater. Interfaces* **2014**, *6*, 12093–12099; c) P. Q. Liao, W. X. Zhang, J. P. Zhang, X. M. Chen, *Nat. Commun.* **2015**, *6*, 8697.
[8] a) R. T. Yang, E. S. Kikkinides, *AIChE J.* **1995**, *41*, 509–517; b) S. Aguado, G. Bergeret, C. Daniel, D. Farrusseng, *J. Am. Chem. Soc.* **2012**, *134*, 14635–14637.
[9] a) Z. B. Bao, S. Alnemrat, L. Yu, I. Vasiliev, Q. L. Ren, X. Y. Lu, S. G. Deng, *Langmuir* **2011**, *27*, 13554–13562; b) B. Li, Y. Zhang, R. Krishna, K. Yao, Y. Han, Z. Wu, D. Ma, Z. Shi, T. Pham, B. Space, J. Liu, P. K. Thallapally, J. Liu, M. Chrzanowski, S. Ma, *J. Am. Chem. Soc.* **2014**, *136*, 8654–8660.
[10] a) E. D. Bloch, W. L. Queen, R. Krishna, J. M. Zadrozny, C. M. Brown, J. R. Long, *Science* **2012**, *335*, 1606–1610; b) S. J. Geier, J. A. Mason, E. D. Bloch, W. L. Queen, M. R. Hudson, C. M. Brown, J. R. Long, *Chem. Sci.* **2013**, *4*, 2054–2061.
[11] a) T. Fukushima, S. Horike, Y. Inubushi, K. Nakagawa, Y. Kubota, M. Takata, S. Kitagawa, *Angew. Chem. Int. Ed.* **2010**, *49*, 4820–4824; *Angew. Chem.* **2010**, *122*, 4930–4934; b) H. Deng, C. J. Doonan, H. Furukawa, R. B. Ferreira, J. Towne, C. B. Knobler, B. Wang, O. M. Yaghi, *Science* **2010**, *327*, 846–850; c) O. Shekhah, Y. Belmabkhout, Z. Chen, V. Guillerm, A. Cairns, K. Adil, M. Eddaoudi, *Nat. Commun.* **2014**, *5*, 4228–4235; d) J. Peng, H. Wang, D. H. Olson, Z. Li, J. Li, *Chem. Commun.* **2017**, *53*, 9332–9335; e) J. An, O. K. Farha, J. T. Hupp, E. Pohl, J. I. Yeh, N. L. Rosi, *Nat. Commun.* **2012**, *3*, 604–609; f) C.-T. He, Z.-M. Ye, Y.-T. Xu, D.-D. Zhou, H.-L. Zhou, D. Chen, J.-P. Zhang, X.-M. Chen, *Chem. Sci.* **2017**, *8*, 7560–7565.
[12] C. C. H. Lin, J. A. Sawada, L. Wu, T. Haastrup, S. M. Kuznicki, *J. Am. Chem. Soc.* **2009**, *131*, 609–614.
[13] a) B. Chen, N. W. Ockwig, A. R. Millward, D. S. Contreras, O. M. Yaghi, *Angew. Chem. Int. Ed.* **2005**, *44*, 4745–4749; *Angew. Chem.* **2005**, *117*, 4823–4827; b) X. Cui, K. Chen, H. Xing, Q. Yang, R. Krishna, Z. Bao, H. Wu, W. Zhou, X. Dong, Y. Han, *Science* **2016**, *353*, 141–144; c) P.-Q. Liao, N.-Y. Huang, W.-X. Zhang, J.-P. Zhang, X.-M. Chen, *Science* **2017**, *356*, 1193–1196; d) J. Li, J. Sculley, H. Zhou, *Chem. Rev.* **2012**, *112*, 869–932; e) Z. Chang, D.-H. Yang, J. Xu, T.-L. Hu, X.-H. Bu, *Adv. Mater.* **2015**, *27*, 5432–5441; f) B. Kesanli, Y. Cui, M. R. Smith, E. W. Bittner, B. C. Bockrath, W. Lin, *Angew. Chem. Int. Ed.* **2005**, *44*, 72–75; *Angew. Chem.* **2005**, *117*, 74–77; g) S.-T. Zheng, J. T. Bu, Y. Li, T. Wu, F. Zuo, P. Feng, X. Bu, *J. Am. Chem. Soc.* **2010**, *132*, 17062–17064; h) R. Vaidhyanathan, S. S. Iremonger, G. K. H. Shimizu, P. G. Boyd, S. Alavi, T. K. Woo, *Science* **2010**, *330*, 650–653; i) J. Wang, D. Xie, Z. Zhang, Q. Yang, H. Xing, Y. Yang, Q. Ren, Z. Bao, *AIChE J.* **2017**, *63*, 2165–2175.
[14] K. J. Chen, D. G. Madden, T. Pham, K. A. Forrest, A. Kumar, Q.-Y. Yang, W. Xue, B. Space, J. J. Perry, J.-P. Zhang, X.-M. Chen, M. J. Zaworotko, *Angew. Chem. Int. Ed.* **2016**, *55*, 10268–10272; *Angew. Chem.* **2016**, *128*, 10424–10428.
[15] R. B. Lin, L. Li, H. Wu, H. Arman, B. Li, R. G. Lin, W. Zhou, B. Chen, *J. Am. Chem. Soc.* **2017**, *139*, 8022–8028.
[16] A. Cadiau, K. Adil, P. M. Bhatt, Y. Belmabkhout, M. Eddaoudi, *Science* **2016**, *353*, 137–140.
[17] A. H. Assen, Y. Belmabkhout, K. Adil, P. M. Bhatt, D.-X. Xue, H. Jiang, M. Eddaoudi, *Angew. Chem. Int. Ed.* **2015**, *54*, 14353–14358; *Angew. Chem.* **2015**, *127*, 14561–14566.
[18] J.-R. Li, R. J. Kuppler, H.-C. Zhou, *Chem. Soc. Rev.* **2009**, *38*, 1477–1504.
[19] a) C. Reid, K. Thomas, *J. Phys. Chem. B* **2001**, *105*, 10619–10629; b) C. E. Webster, R. S. Drago, M. C. Zerner, *J. Am. Chem. Soc.* **1998**, *120*, 5509–5516.
[20] a) L. Cooper, T. Hidalgo, M. Gorman, T. Lozano-Fernandez, R. Simon-Vazquez, C. Olivier, N. Guillou, C. Serre, C. Martineau, F. Taulelle, D. Damasceno-Borges, G. Maurin, A. Gonzalez-Fernandez, P. Horcajada, T. Devic, *Chem. Commun.* **2015**, *51*,

5848 – 5851; b) R. K. Feller, A. K. Cheetham, *Solid State Sci.* **2006**, *8*, 1121 – 1125.
[21] S. H. Hyun, R. P. Danner, *J. Chem. Eng. Data* **1982**, *27*, 196 – 200.
[22] Y. He, R. Krishna, B. Chen, *Energy Environ. Sci.* **2012**, *5*, 9107 – 9120.
[23] S. Yang, A. J. Ramirez-Cuesta, R. Newby, V. Garcia-Sakai, P. Manuel, S. K. Callear, S. I. Campbell, C. C. Tang, M. Schroder, *Nat. Chem.* **2015**, *7*, 121 – 129.
[24] M. Mofarahi, S. M. Salehi, *Adsorption* **2013**, *19*, 101 – 110.
[25] B. Saccoccia, A. M. Bohnsack, N. W. Waggoner, K. H. Cho, J. S. Lee, D. Y. Hong, V. M. Lynch, J. S. Chang, S. M. Humphrey, *Angew. Chem. Int. Ed.* **2015**, *54*, 5394 – 5398; *Angew. Chem.* **2015**, *127*, 5484 – 5488.

Manuscript received: July 29, 2018
Revised manuscript received: October 9, 2018
Accepted manuscript online: October 10, 2018
Version of record online: November 11, 2018

Angewandte Chemie
Eine Zeitschrift der Gesellschaft Deutscher Chemiker

Supporting Information

Molecular Sieving of Ethane from Ethylene through the Molecular Cross-Section Size Differentiation in Gallate-based Metal–Organic Frameworks

Zongbi Bao, Jiawei Wang, Zhiguo Zhang, Huabin Xing, Qiwei Yang, Yiwen Yang, Hui Wu, Rajamani Krishna, Wei Zhou, Banglin Chen,* and Qilong Ren**

anie_201808716_sm_miscellaneous_information.pdf

SUPPORTING INFORMATION

Methods:

Materials

$MgCl_2$ was purchased from Alfa Aesar Co. (USA). $CoCl_2 \cdot 6H_2O$, $NiCl_2 \cdot 6H_2O$, $Ni(CH_3COO)_2 \cdot 4H_2O$, gallic acid monohydrate and hydroxypropyl cellulose were obtained from Sigma-Aldrich Co. (USA). All chemicals were directly used without further purification. High-purity gases including C_2H_4 (99.99%), C_2H_6 (99.99%), N_2 (99.999%), He (99.999%) and mixed gases of C_2H_4/C_2H_6 = 50/50 were provided by Jingong Co., Ltd. (China).

Synthesis of M-gallate (M= Ni, Mg, Co)

The synthesis of M-gallate was carried out as previously reported method.[1] Metal chloride (2 mmol) and gallic acid monohydrate (H_4gal, 4 mmol) were mixed in 10 mL KOH aqueous solution (0.16 M for Ni, Co-gallate, 0.5 M for Mg-gallate). After ultrasonic treatment for 30 min, the mixture was sealed in a Teflon-lined stainless steel autoclave and heated at 120 °C under autogenous pressure for 24 h. The autoclave was cooled down at room temperature and the obtained powder was washed with water followed by absolute ethanol. The sample was activated at 120 °C for 24 h under ultrahigh vacuum before single-component gas adsorption and breakthrough tests.

Synthesis of Ni-gallate single crystal

The synthesis of single crystal of Ni-gallate was carried out by the following method. $Ni(CH_3COO)_2 \cdot 4H_2O$ (150 mg) and gallic acid monohydrate (H_4gal, 188 mg) were mixed in 10 mL H_2O. After ultrasonic treatment for 30 min, the mixture was sealed in a Teflon-lined stainless steel autoclave and heated at 110 °C under autogenous pressure for 72 h, then slowly cooled to room temperature in 24 h. The size of obtained single crystal is larger than 200 μm.

Scale-up synthesis of Mg-gallate

For scale up, 50 mmol $MgCl_2$ and 100 mmol gallic acid monohydrate were added to 250 mL 0.5 M KOH aqueous solution in a three-necked flask. Then the mixture was heated and refluxed at 80 °C and ambient pressure for 24 h with continuous stirring. After cooling down, the product was collected and washed with H_2O and ethanol successively.

Preparation of Mg-gallate extrudates

In the process of molding, hydroxypropyl cellulose (HPC) was used as the binder. 0.5 g Mg-gallate powder, 25 mg HPC, and 0.3 mL H_2O were mixed uniformly to form a paste. The paste was partially dried at ambient temperature and then passed through hollow plastic tube of a 1 mL injection syringe. The spaghetti-like noodles were placed on a piece of tin foil sheet and semi-dried at room temperature for about 20

minutes. The dried noodles were then cut into tablets with dimension of 2 × 2 mm in diameter and length.

Determination of BET surface area

The BET surface area of M-gallate was characterized by CO_2 adsorption-desorption isotherms at 195 K. The adsorption-desorption isotherms were both obtained on a Micromeritics ASAP 2460 (Micromeritics Instrument Corp., USA). Each sample was degassed at 120 ºC for 24 h under ultrahigh vacuum before measurement. The BET surface area is calculated by the reported method[2].

Determination of crystal structure of Ni-gallate

The diffraction data of Ni-gallate was collected on a Rigaku XtaLAB MM007 CCD diffractometer at 100 K with Cu Kα radiation (λ= 1.5418 Å) by scan mode. The structure was solved by direct methods using the SHELXTL[3] program and refined by full-matrix least-squares methods with SHELXL. Metal atoms were located from the *E*-maps and other non-hydrogen atoms were located from the successive difference Fourier syntheses and refined with anisotropic thermal parameters on F^2. The H atoms of the coordinated water molecules in Ni-gallate cannot be added in the calculated positions, and they were directly included in the final molecular formula. Detailed crystallographic data is summarized in Table S1.

Powder X-ray diffraction analysis

Powder X-ray diffraction (PXRD) patterns of the samples were recorded with an XPert diffractometer (Panalytical Corp., Netherlands) using Cu Kα (λ=0.1543 nm) radiation at 40 kV from 5º to 50º (2θ angle range) with a step size of 0.02º.

Thermal gravimetric analysis

Thermal gravimetric analysis (TGA) was performed in a TA-Q500 TGA instrument (TA Instruments Corp., USA) from 50 to 600 ºC in air atmosphere at a constant rate of 5 ºC/min.

Gas adsorption measurement

The sample of M-gallate was degassed at 120 ºC for 24 h under ultrahigh vacuum, then the single-component isotherms for both ethane and ethylene at 273, 298, and 313 K were measured on a Micromeritics ASAP 2460 gas adsorption analyzer.

Breakthrough experiments

The M-gallate was first activated under ultrahigh vacuum at 120 ºC for 24 h. As shown in Scheme S1, breakthrough tests were conducted in a stainless steel column (50 mm × 4.6 mm ID) manually packed with activated samples (Ni-gallate: 0.72 g; Mg-gallate: 0.37 g; Co-gallate: 0.58 g). The binary mixture of C_2H_4/C_2H_6 (50/50, *v/v*) was introduced with a constant flow rate of 0.5 mL/min at 273 K. The outlet gas from the column was monitored using a GC-2010 plus (SHIMADZU) gas chromatography

with a flame ionization detector (FID) and a thermal conductivity detector (TCD). After the breakthrough tests, the column was regenerated with a He flow at 120 °C for 24 hours.

The dynamic saturated adsorption capacity of gas *i* (q_i) is calculated from the breakthrough curve by the equation

$$q_i = \frac{F_i \cdot t_0 - V_{dead} - \int_0^{t_0} F_e \Delta t}{m}$$

where F_i is the influent flow rate of the specific gas (cm^3/min); t_0 is the adsorption time (min); V_{dead} is the dead volume of the system (cm^3); F_e is the effluent flow rate of the specific gas (cm^3/min); and m is the mass of the adsorbent (g).

Neutron diffraction experiment

Neutron powder diffraction data were collected using the BT-1 neutron powder diffractometer at the NIST Center for Neutron Research. A Ge(311) monochromator with a 75° take-off angle, *lambda* = 2.0787(2) Å, and in-pile collimation of 60 minutes of arc were used. Data were collected over the range of 1.3-166.3° *2-Theta* with a step size of 0.05°. Fully activated Mg-gallate sample was loaded in a vanadium can equipped with a capillary gas line and a packless valve. The bare Mg-gallate sample was measured first at 200 K. To probe the gas adsorption structure, C_2D_4 was loaded into the sample at room temperature and equilibrated at ~0.1 bar. (Note: deuterated gas C_2D_4 was used to avoid the large incoherent neutron scattering background that would be produced by the hydrogen in C_2H_4.) Then, the sample was slowly cooled to 200 K, and subsequently diffraction data were collected.

Rietveld structural refinements were performed on the diffraction data using the GSAS package.[4] Due to the large number of atoms in the crystal unit cell, the ligand molecule and the gas molecule were both treated as rigid bodies in the Rietveld refinement (to limit the number of variables), with the molecule orientation and center of mass freely refined. Final refinement on the positions/orientations of the rigid bodies, thermal factors, occupancies, lattice parameters, background, and profiles converges with satisfactory *R*-factors.

Dual-Langmuir-Freundlich fits for single-component isotherms

The isotherm data for C_2H_4, and C_2H_6 in M-gallate were measured at three different temperatures 273 K, 298 K, and 313 K. The unary isotherm data were fitted with the Dual-site Langmuir-Freundlich model

$$q = q_{A,sat} \frac{b_A p^{\nu_A}}{1 + b_A p^{\nu_A}} + q_{B,sat} \frac{b_B p^{\nu_B}}{1 + b_B p^{\nu_B}}$$

The Langmuir parameters for each site is temperature-dependent

$$b_A = b_{A0} \exp\left(\frac{E_A}{RT}\right); \quad b_b = b_{B0} \exp\left(\frac{E_B}{RT}\right)$$

The dual-site Langmuir-Freundlich parameters are provided in Tables S4-S6. For all guest/host combinations the unary fits are excellent.

IAST calculations of adsorption selectivities

The adsorption selectivities were established by the Ideal Adsorbed Solution Theory (IAST)[5] for C_2H_4/C_2H_6 (50/50, *v/v*) binary mixtures in M-gallate. The adsorption selectivity, S_{ij}, is defined by the following equation

$$S_{ij} = \frac{x_i / x_j}{y_i / y_j}$$

where x_i and x_j are the equilibrated adsorption capacity of component *i* and *j*, respectively; and y_i and y_j are the molar fractions of component *i* and *j* in gas phase, respectively.

Isosteric heat of adsorption

The binding energy of C_2H_4 are reflected in the isosteric heat of adsorption, Q_{st}, defined as

$$Q_{st} = \mathrm{R}T^2 \left(\frac{\partial lnp}{\partial T}\right)$$

Figure S8 presents the isosteric heat of adsorption of C_2H_4 and C_2H_6 for M-gallate, which were determined using the pure component isotherm fits using Clausius-Clapeyron equation.

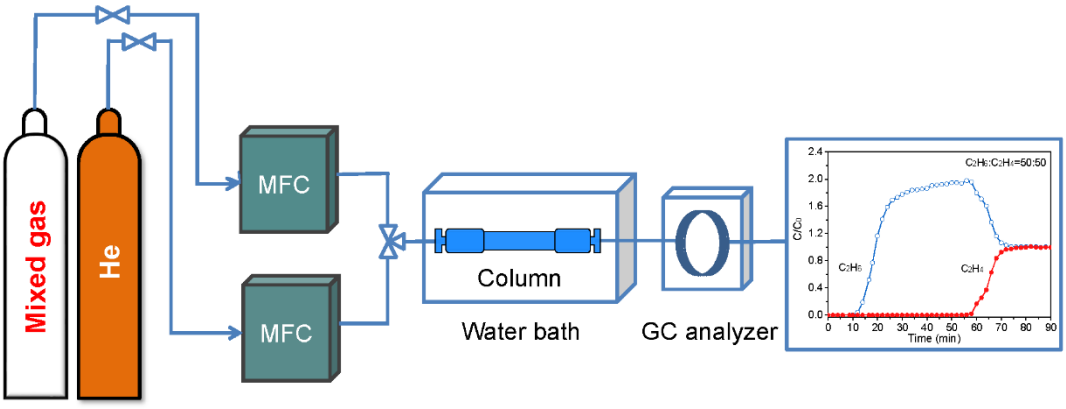

Scheme S1. Schematic diagram for C_2H_4/C_2H_6 mixed gas breakthrough tests.

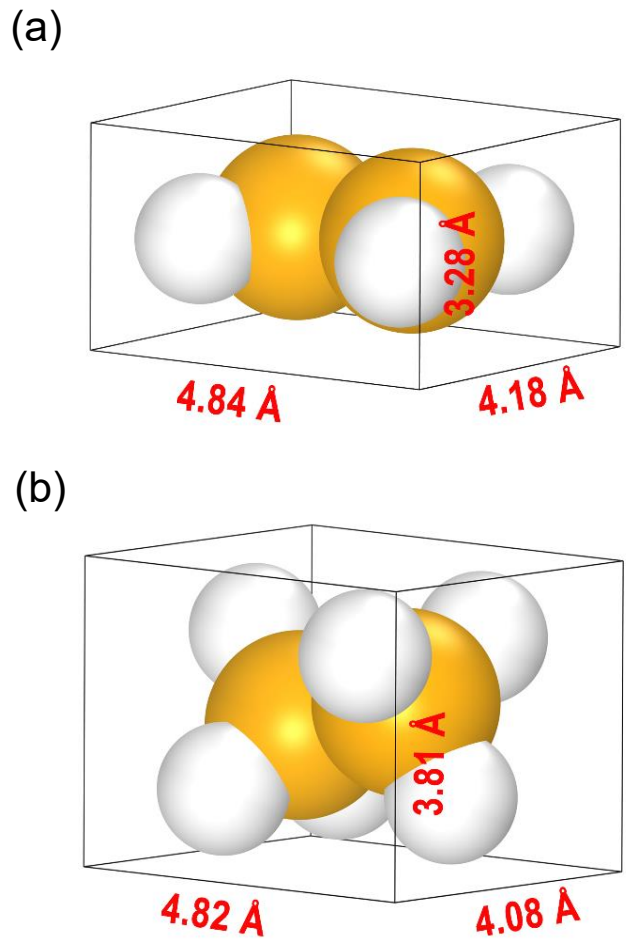

Figure S1. Van der Waals molecular dimensions of (a) C_2H_4 (3.28 × 4.18 × 4.84 $Å^3$) and (b) C_2H_6 (3.81 × 4.08 × 4.82 $Å^3$). The dimensions of the molecule along the x, y, and z symmetry axes of the molecule were calculated for each atom surrounded by a van der Waal sphere. The van der Waal radii of the corresponding atoms were 1.20 and 1.70 Å for H atom and C atom, respectively. The minimum molecular cross section of C_2H_4 and C_2H_6 are 3.28 × 4.18 and 3.81 × 4.08 $Å^2$, respectively; In contrast, the kinetic diameters of these two molecules are 4.16 and 4.44 Å, respectively.

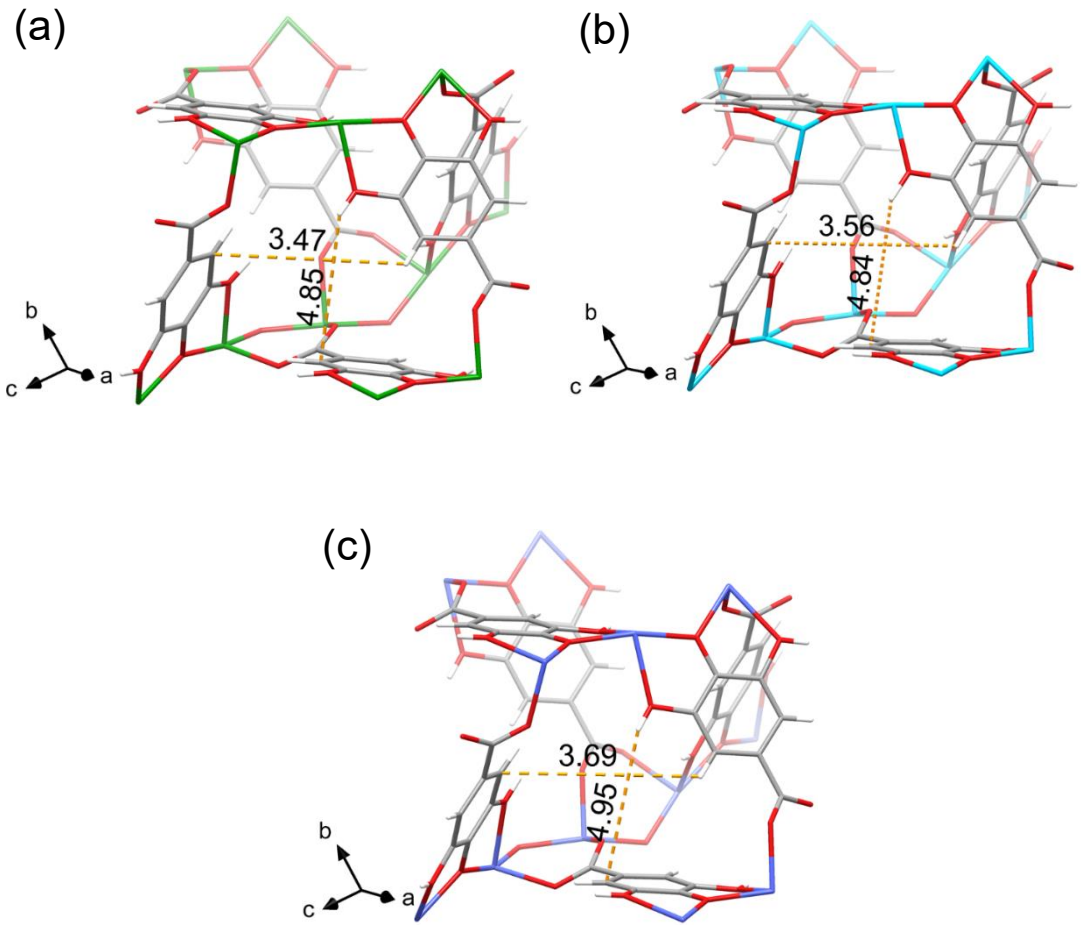

Figure S2. Quasi-discrete cavities are interconnected by narrow windows of (a) 3.47 × 4.85 Å^2 for Ni-gallate, (b) 3.56 × 4.84 Å^2 for Mg-gallate, and (c) 3.69 × 4.95 Å^2 for Co-gallate. The radiuses of hydrogen and carbon atom have been subtracted.

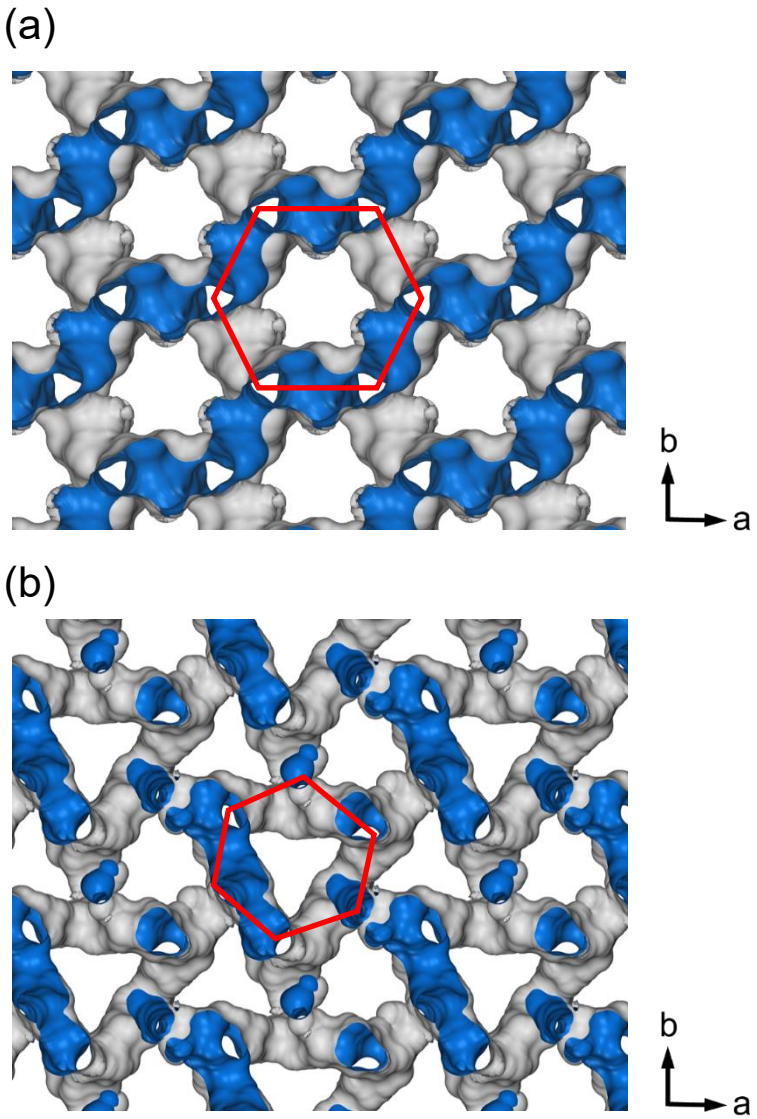

Figure S3. Calculated pore surface and zigzag channels of (a) M-gallate·2H_2O. The free water molecules are omitted for clarity. (b) Dehydrated M-gallate. The crystal structure of M-gallate becomes slightly disordered and changes from $P3_221$ to P31 space group after activation, leading to a modest change of the pore structure and size.

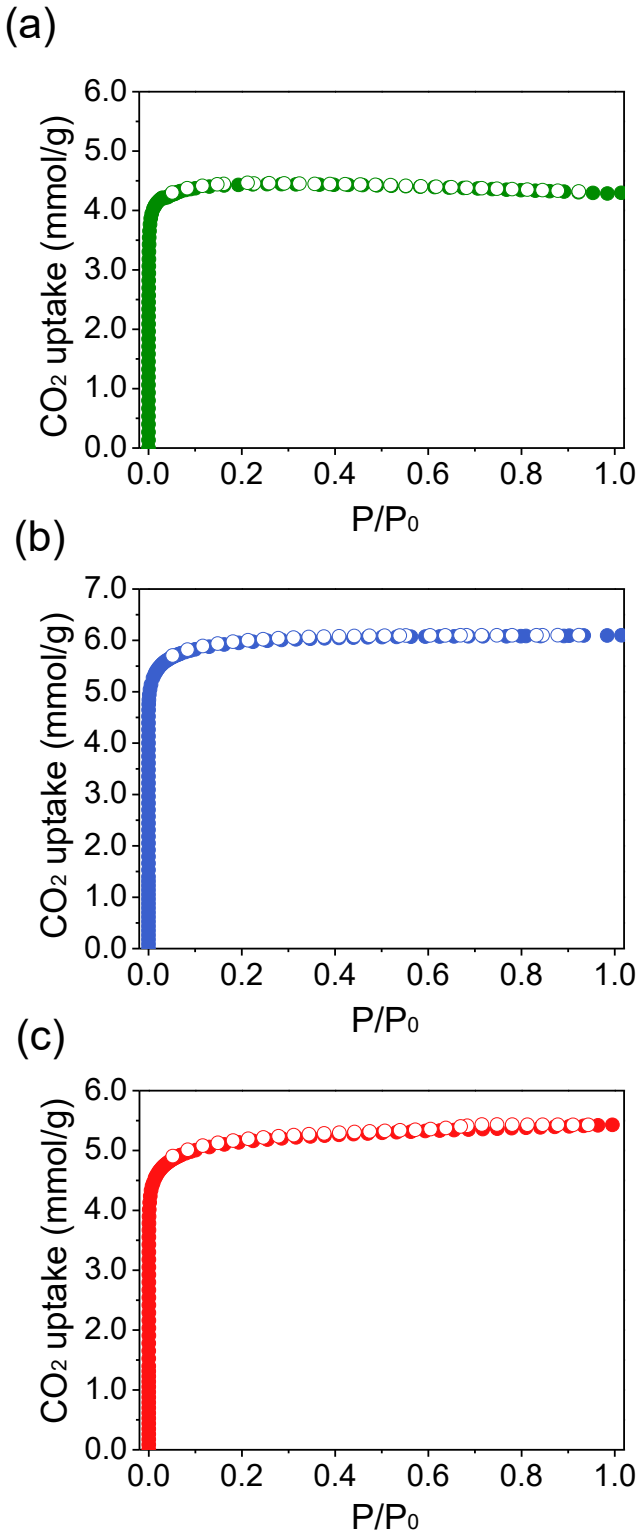

Figure S4. CO_2 adsorption isotherms at 195 K for (a) Ni-gallate, (b) Mg-gallate, and (c) Co-gallate. The calculated BET surface area is 424, 559, and 475 m^2/g for Ni, Mg, Co-gallate, respectively.

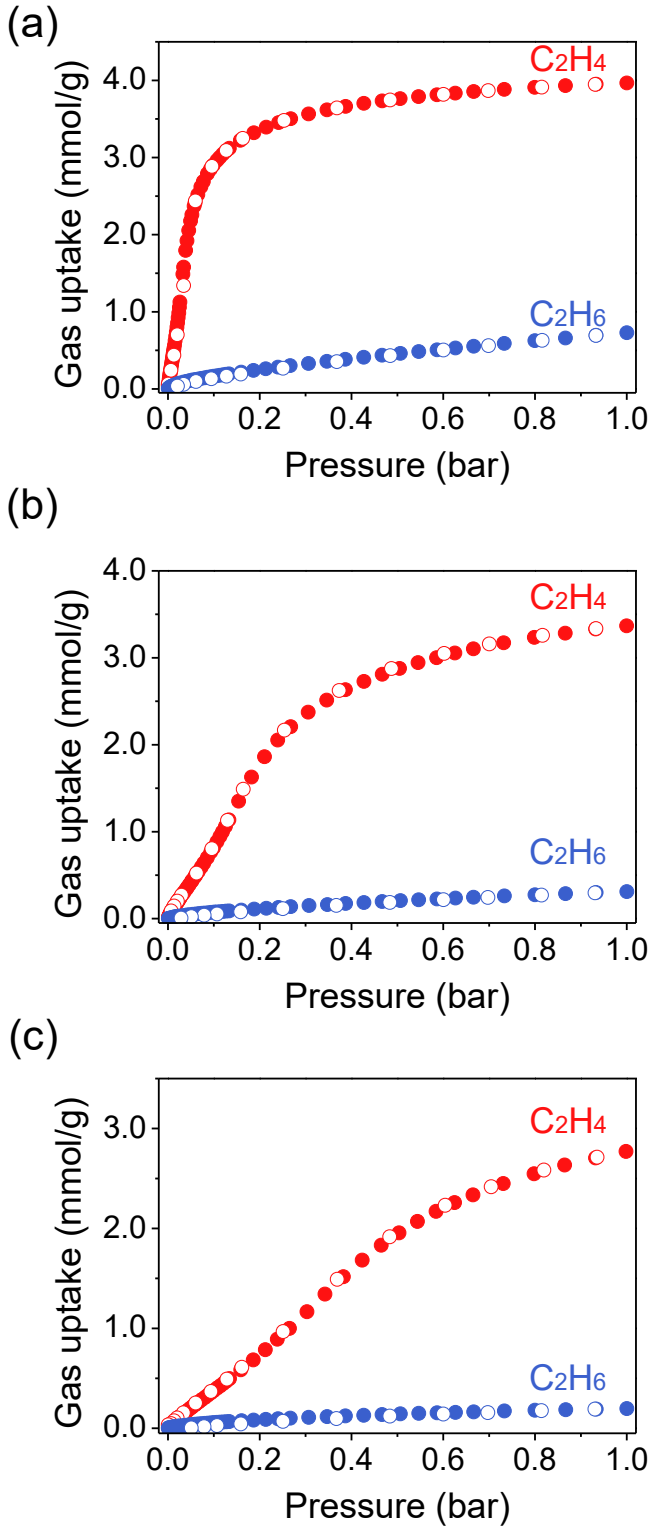

Figure S5. Single-component adsorption isotherms for C_2H_4 and C_2H_6 for Co-gallate (a: 273 K, b: 298 K, c: 313 K).

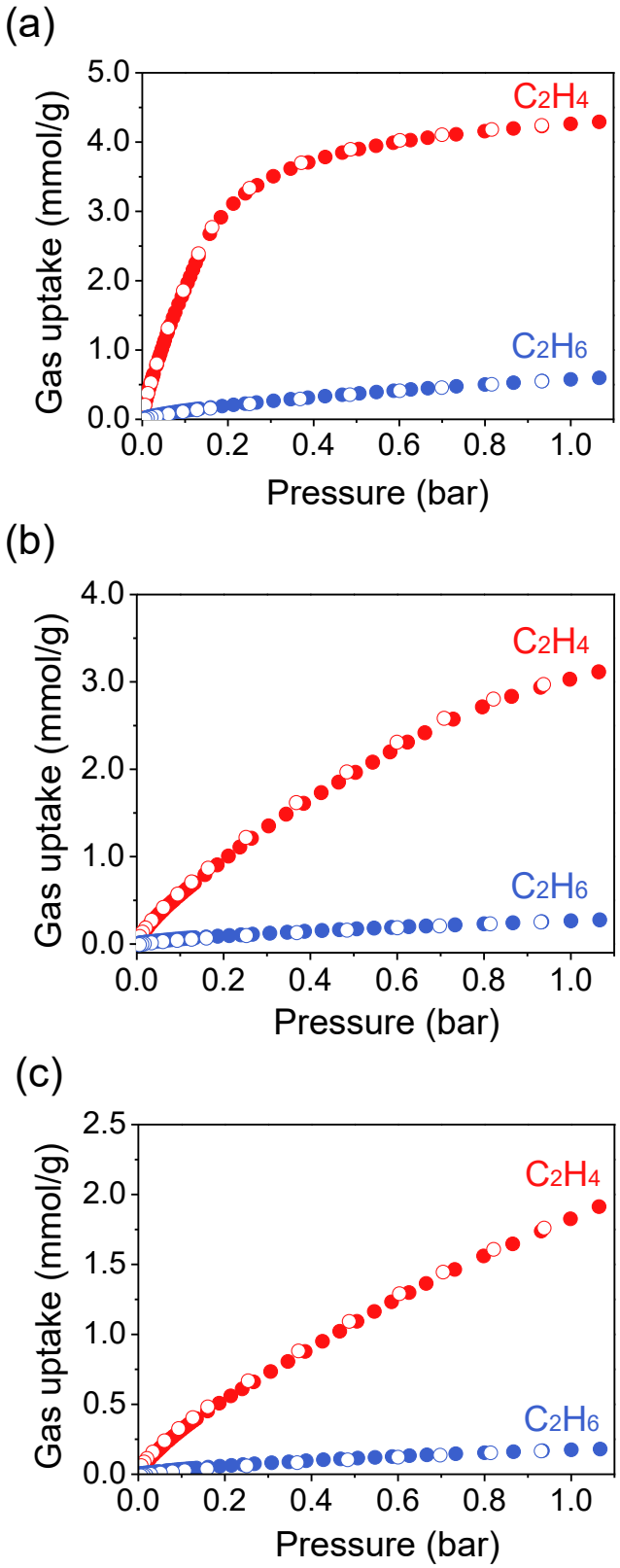

Figure S6. Single-component adsorption isotherms for C_2H_4 and C_2H_6 for Mg-gallate (a: 273 K, b: 298 K, c: 313 K).

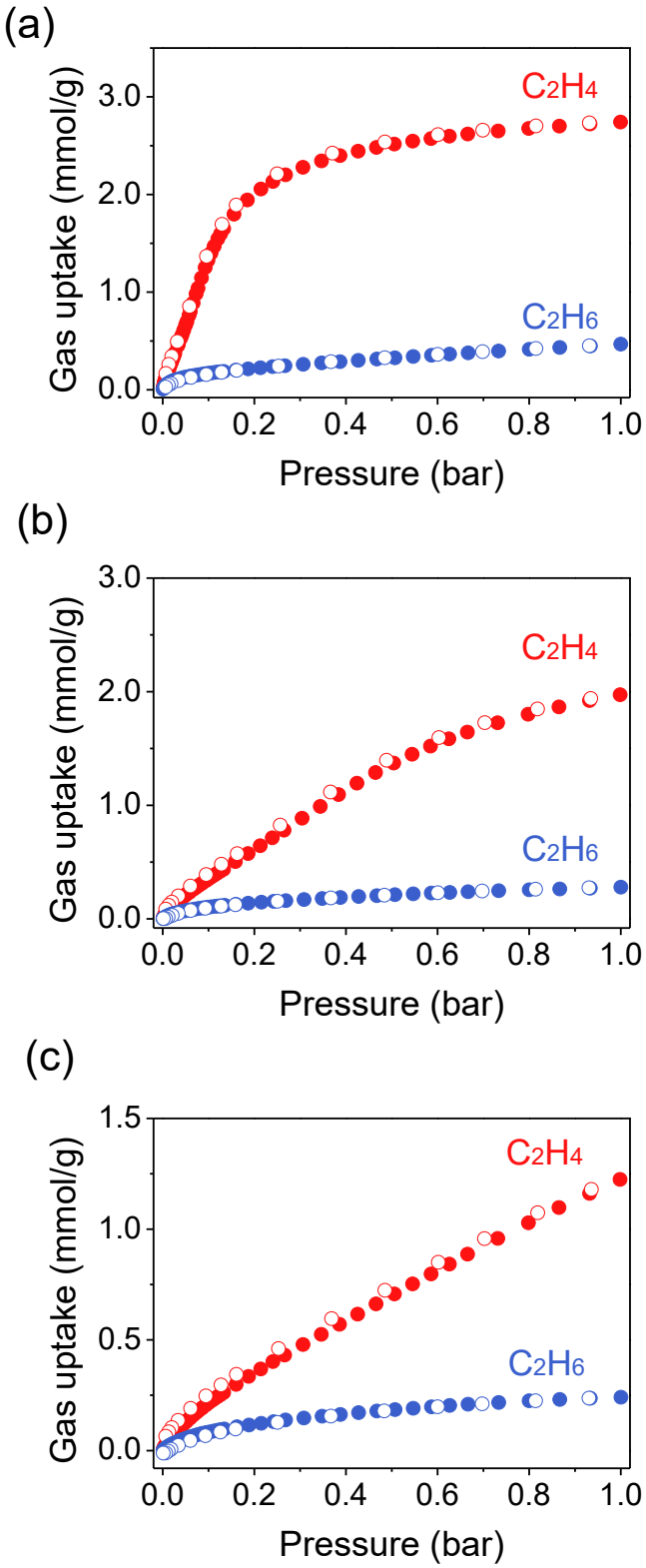

Figure S7. Single-component adsorption isotherms for C_2H_4 and C_2H_6 for Ni-gallate (a: 273 K, b: 298 K, c: 313 K).

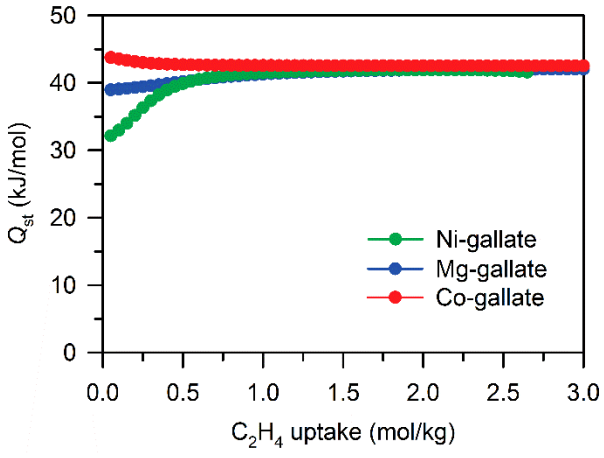

Figure S8. Q_{st} of C_2H_4 adsorption in M-gallate.

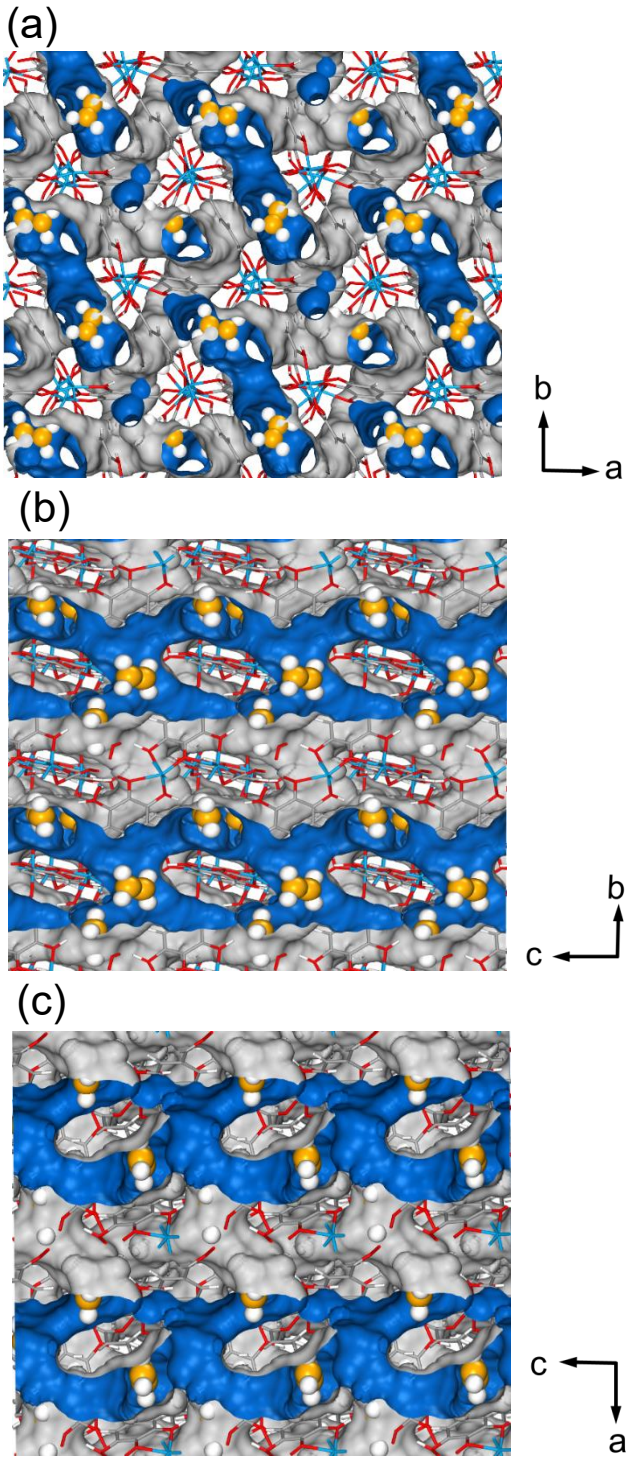

Figure S9. Stacking diagram of the Mg-gallate·C_2D_4 along (a) c axis, (b) a axis, and (c) b axis. The Connolly surface is calculated with a Connolly radius of 1.0 Å.

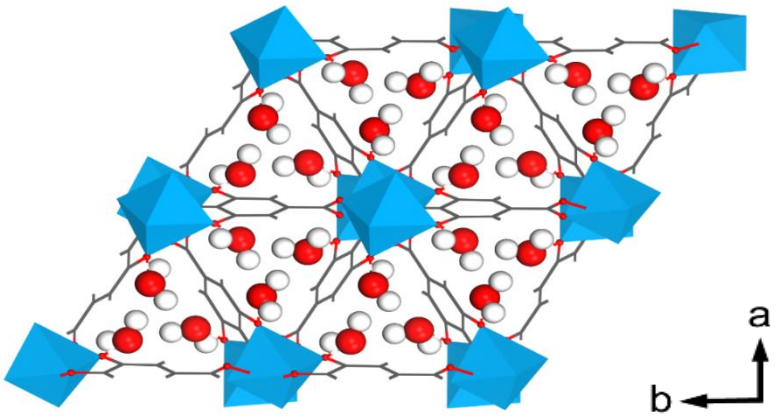

Figure S10. Structure of Mg-gallate·$2H_2O$ along with c axis. The free water molecules are located within the c-axis straight channels. Mg, C, O, H in Mg-gallate are represented by cyan, grey, red and white, respectively.

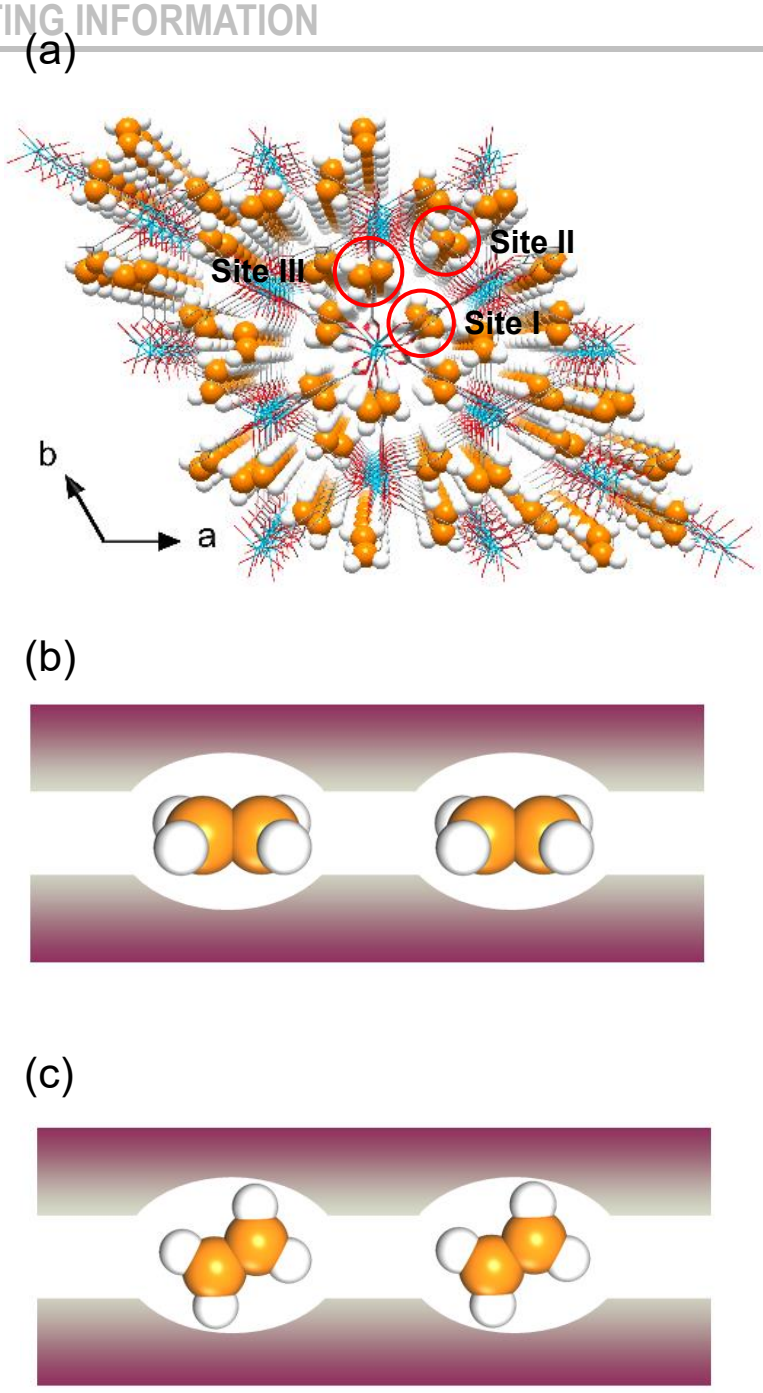

Figure S11. (a) Neutron diffraction crystal structure of Mg-gallate·C_2D_4. The three adsorption binding sites in Mg-gallate are labeled as Site I, Site II, and Site III. (b,c) Schematic diagram of the three C_2H_4 adsorption binding sites (b: Site I and III; c: Site II) in the fusiform branched channels.

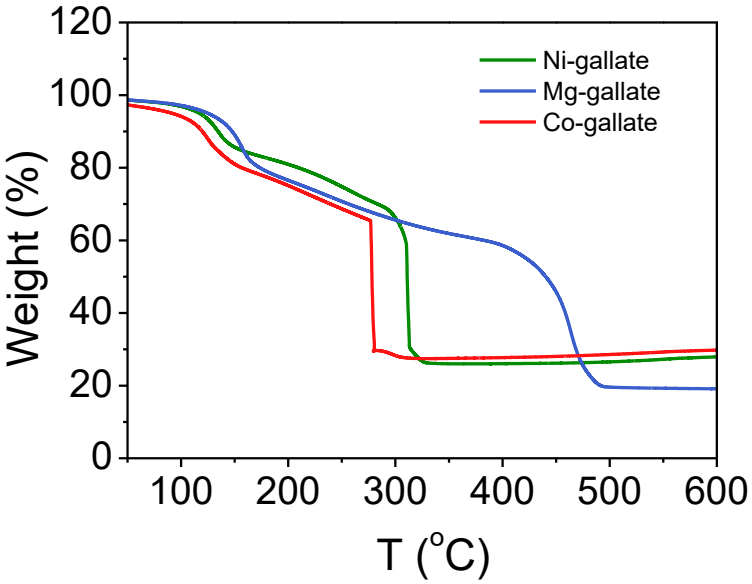

Figure S12. TGA curves for Co, Mg, Ni-gallate.

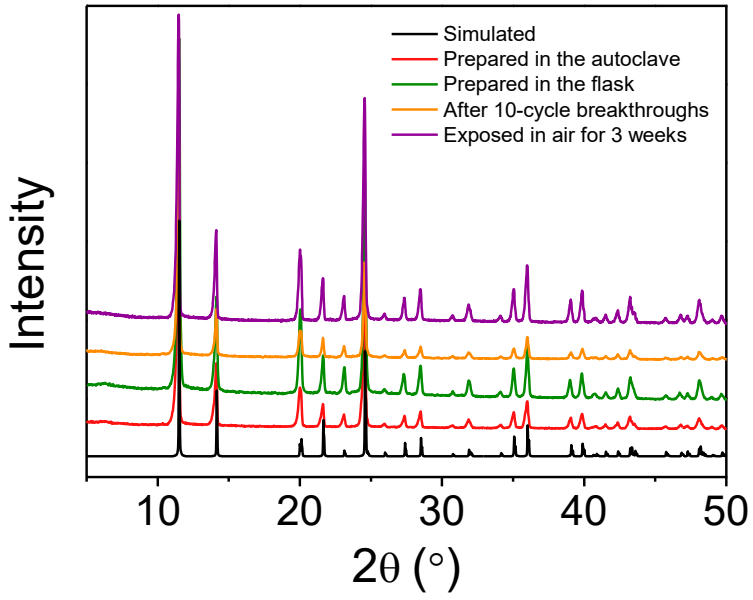

Figure S13. Powder X-ray diffraction patterns of various Mg -gallate samples.

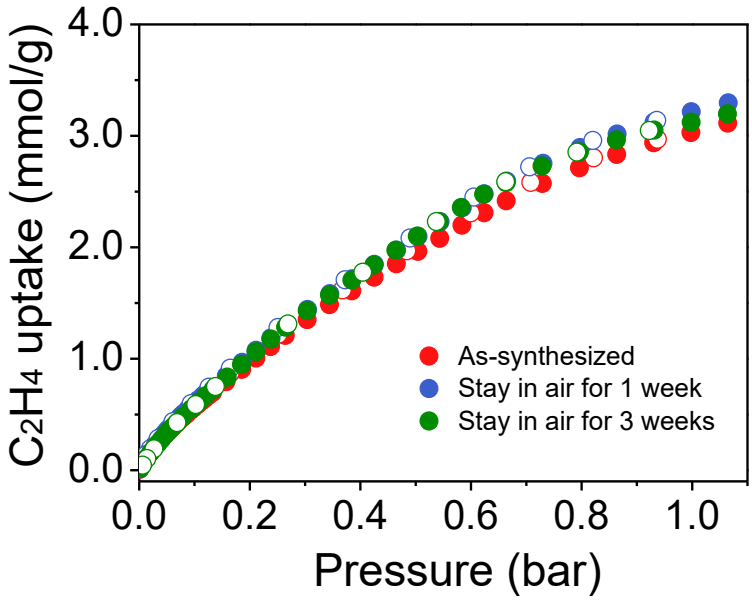

Figure S14. Single-component adsorption isotherms of C_2H_4 of samples as-synthesized, exposed in air for 1 week and 3 weeks respectively at 298 K for Mg-gallate.

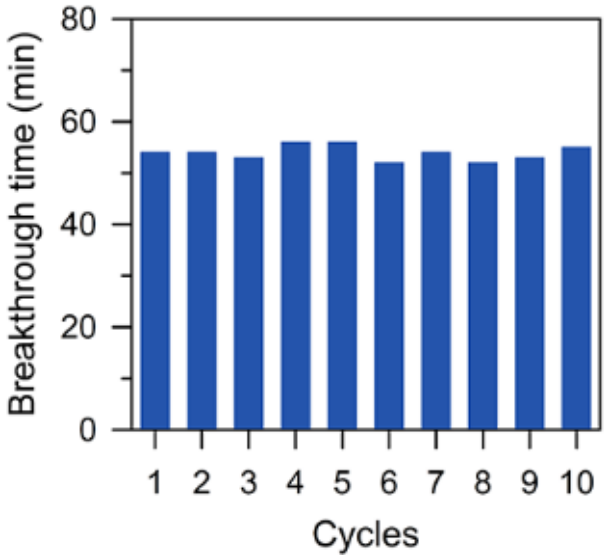

Figure S15. C_2H_4/C_2H_6 binary mixture (50/50, *v/v*) 10 cyclic experiments for Mg-gallate at 273 K and 1 bar with a flow rate of 0.5 mL/min. The column was reactivated with a helium flow at 120 ºC after every breakthrough test.

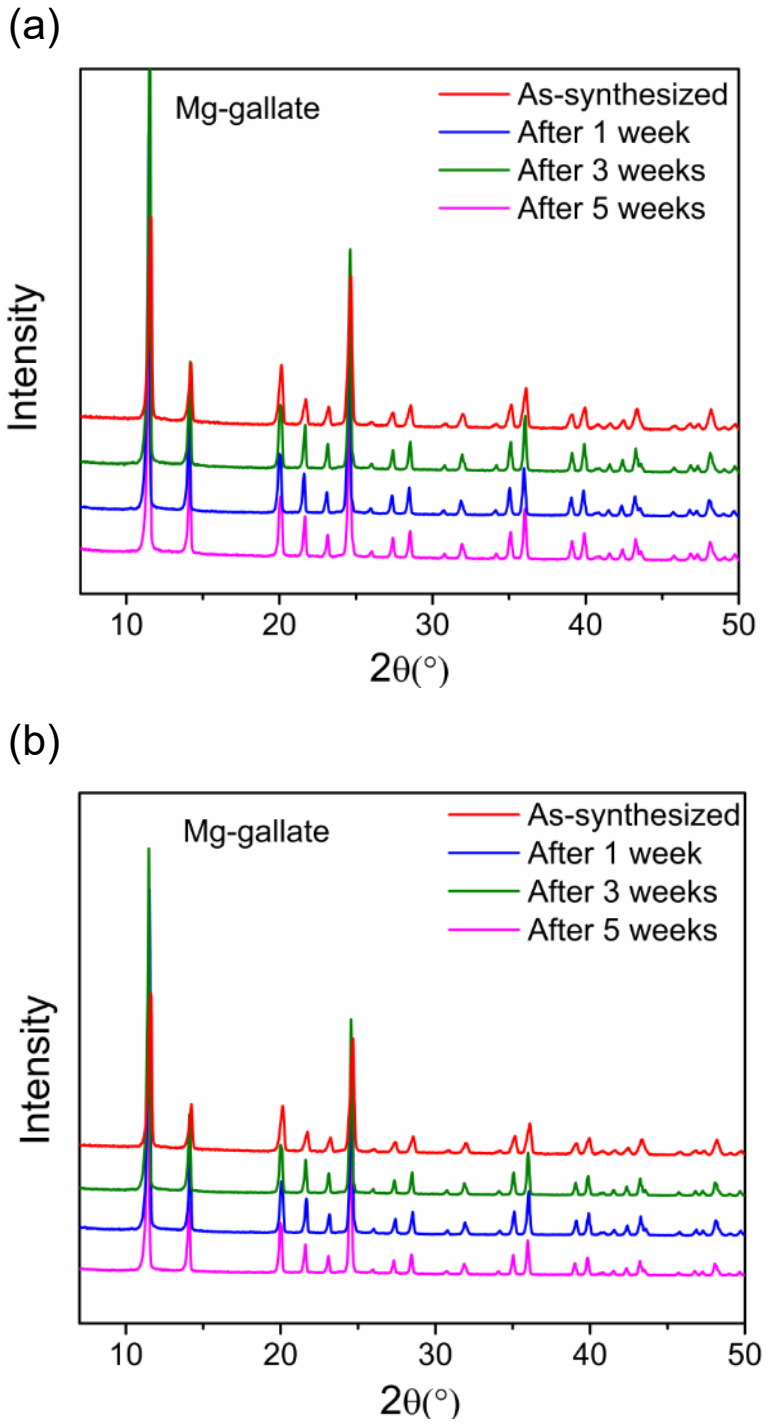

Figure S16. Powder X-ray diffraction patterns of Mg -gallate samples after soaked in (a) water and (b) ethanol for 1, 3, and 5 weeks, respectively.

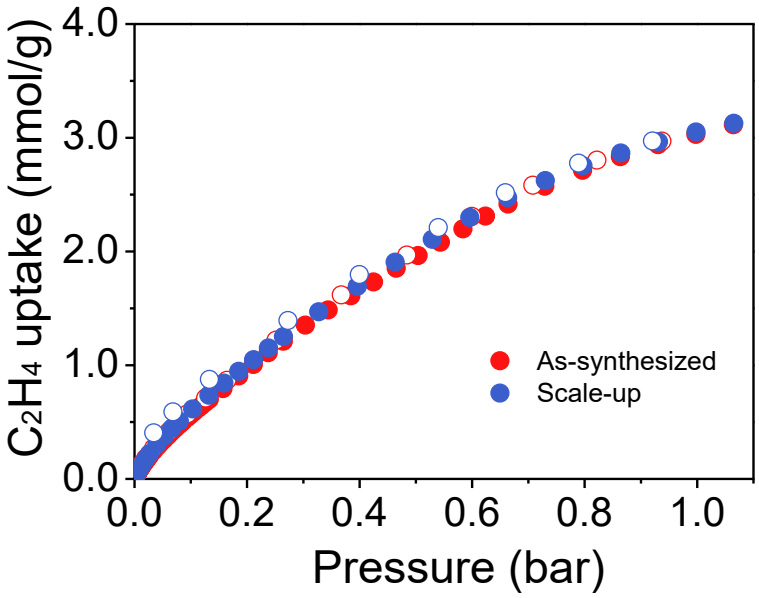

Figure S17. Comparison of the single-component adsorption isotherms of C_2H_4 for as-synthesized (red) and scale-up (blue) Mg-gallate at 298 K.

Figure S18. The photographs of molded Mg-gallate (left) and molded UOP zeolite 13X (right).

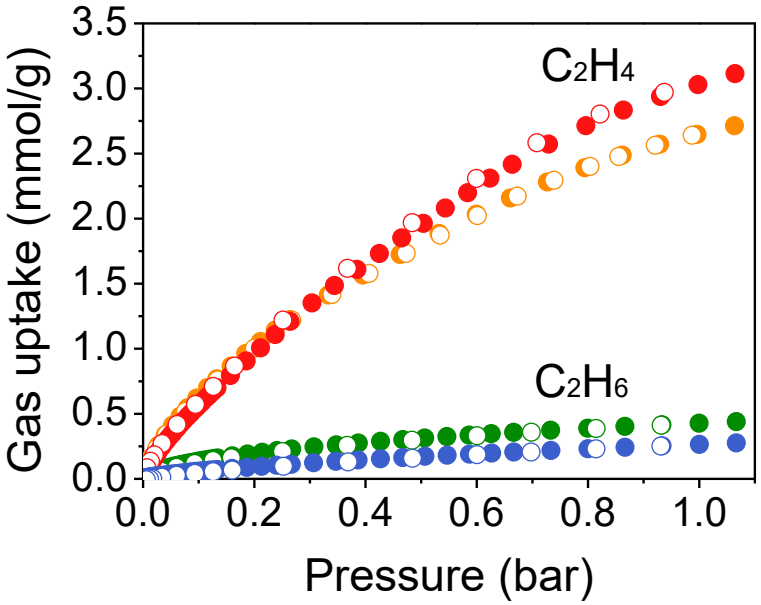

Figure S19. Comparison of the single-component adsorption isotherms of C_2H_4 and C_2H_6 for molded Mg-gallate (orange for C_2H_4, green for C_2H_6) and original Mg-gallate (red for C_2H_4, blue for C_2H_6) at 298 K.

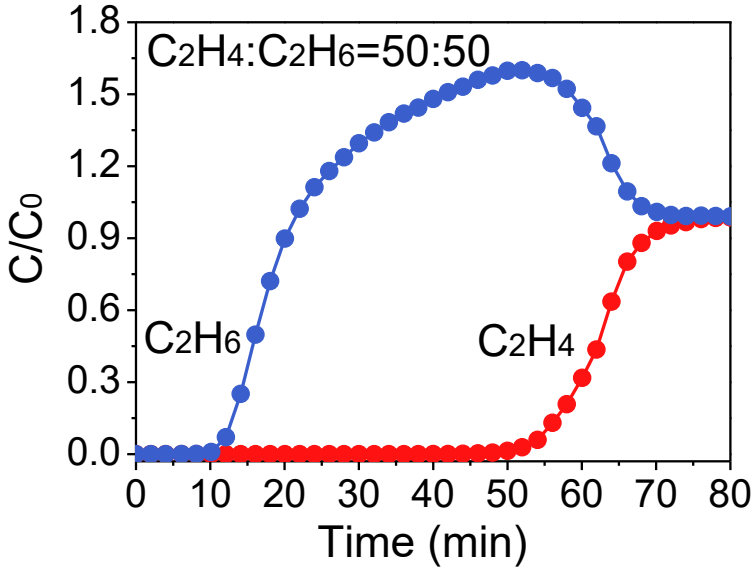

Figure S20. Experimental breakthrough curves for molded Mg-gallate for C_2H_4/C_2H_6 (50/50, *v/v*) binary mixture with a constant flow rate of 0.5 mL/min at 273 K. The column (50 mm × 4.6 mm ID) was packed with 0.37 g samples.

Table S1. Crystal data and structure of Ni-gallate·2H_2O, Mg-gallate·2H_2O, and Co-gallate·2H_2O.

Crystals	Ni-gallate·2H_2O	Mg-gallate·2H_2O	Co-gallate·2H_2O
Formula	$C_7H_8NiO_7$	$C_7H_8MgO_7$	$C_7H_8CoO_7$
Formula weight	262.84	228.44	263.08
Crystal system	Trigonal	Trigonal	Trigonal
Space group	$P3_221$ (154)	$P3_221$ (154)	$P3_221$ (154)
a (Å)	8.81	8.87	8.93
b (Å)	8.81	8.87	8.93
c (Å)	10.60	10.77	10.67
α (º)	90	90	90
β (º)	90	90	90
γ (º)	120	120	120
Cell volume (Å^3)	711.94	733.83	736.12
Z	3	3	3
Calc. density (g/cm^3)	1.80	1.904	2.13

Table S2. Crystal data and structure of Mg-gallate, and Mg-gallate·C_2D_4.

Crystals	Mg-gallate	Mg-gallate·C_2D_4
Formula	$C_7H_4MgO_5$	$C_{7.97}H_4D_{1.93}MgO_5$
Formula weight	192.41	207.92
Crystal system	Trigonal	Trigonal
Space group	P31 (144)	P31 (144)
a (Å)	15.11	15.27
b (Å)	15.11	15.27
c (Å)	10.30	10.32
α (º)	90	90
β (º)	90	90
γ (º)	120	120
Cell volume ($Å^3$)	2037.16	2083.16
Z	9	9
Calc. density (g/cm^3)	1.411	1.492

Table S3. Summary of the gas uptakes, selectivities and Q_{st} for C_2H_4, C_2H_6 in various porous materials.

	Surface area (m^2/g)	Pore size ($Å^2$)	Framework density (g/cm^3)	C_2H_4 uptake* (mmol/g)	Volumetric C_2H_4 uptake* (mmol/mL)&	C_2H_6 uptake* (mmol/g)	Selectivity for $C_2H_4/C_2H_6$$	Q_{st} of C_2H_4# (kJ/mol)
Zeolite 13X[6]	950	~10	1.421	2.77	3.94	2.21	13.4	39
FeMOF-74[7]	1350	11 × 11	1.126	6.1	6.87	5.0	13.6	45
NOTT-300[8]	1370	6.5 × 6.5	1.146	4.28	4.90	0.85	48.7	16
Ni-gallate	424	3.47 × 4.85	1.589	1.97	3.13	0.28	16.8	32
Mg-gallate	559	3.56 × 4.84	1.411	3.03	4.28	0.26	37.3	39
Co-galalte	475	3.69 × 4.95	1.536	3.37	5.18	0.31	52	44

The data was collected at 318 K for FeMOF-74, 298 K for zeolite 13X and M-gallate, and 293 K for NOTT-300.

* Gas uptakes at 1 bar.

&The volumetric C_2H_4 uptake is estimated based on their densities calculated from the crystal structures.

$ IAST selectivity for equimolar C_2H_4/C_2H_6 mixture at 298 K and 1 bar.

Q_{st} at low coverage.

Table S4. *T*-dependent dual-site Langmuir-Freundlich fit parameters for C_2H_4 and C_2H_6 in Ni-gallate at 298 K.

	Site A				Site B			
	$q_{A,sat}$	b_{A0}	E_A	v_A	$q_{B,sat}$	b_{B0}	E_B	v_B
	mol kg^{-1}	Pa$^{-v_A}$	kJ mol^{-1}	dimensionless	mol kg^{-1}	Pa$^{-v_B}$	kJ mol^{-1}	dimensionless
C_2H_4	2.3	1.81E-21	72	1.7	0.45	2.14E-09	29	0.92
C_2H_6	0.2	4.30E-09	27.3	0.9	1.05	1.09E-11	26	1.1

Table S5. *T*-dependent dual-site Langmuir-Freundlich fit parameters for C_2H_4 and C_2H_6 in Mg-gallate at 298 K.

	Site A				Site B			
	$q_{A,sat}$	b_{A0}	E_A	v_A	$q_{B,sat}$	b_{B0}	E_B	v_B
	mol kg^{-1}	Pa$^{-v_A}$	kJ mol^{-1}	dimensionless	mol kg^{-1}	Pa$^{-v_B}$	kJ mol^{-1}	dimensionless
C_2H_4	3.3	1.34E-21	72	1.7	1.1	1.32E-10	35	0.9
C_2H_6	0.2	5.51E-8	21.5	0.7	2.6	1.80E-11	29	0.9

Table S6. *T*-dependent dual-site Langmuir-Freundlich fit parameters for C_2H_4 and C_2H_6 in Co-gallate at 298 K.

	Site A				Site B			
	$q_{A,sat}$	b_{A0}	E_A	v_A	$q_{B,sat}$	b_{B0}	E_B	v_B
	mol kg^{-1}	Pa$^{-v_A}$	kJ mol^{-1}	dimensionless	mol kg^{-1}	Pa$^{-v_B}$	kJ mol^{-1}	dimensionless
C_2H_4	3.5	1.66E-20	71	1.67	0.3	7.86E-12	44	1
C_2H_6	0.1	7.70E-08	22	0.8	4.5	1.19E-11	30	0.88

References

[1] a) L. Cooper, T. Hidalgo, M. Gorman, T. Lozano-Fernandez, R. Simon-Vazquez, C. Olivier, N. Guillou, C. Serre, C. Martineau, F. Taulelle, D. Damasceno-Borges, G. Maurin, A. Gonzalez-Fernandez, P. Horcajada, T. Devic, *Chem. Commun.* **2015**, *51*, 5848-5851; b) R. K. Feller, A. K. Cheetham, *Solid State Sci.* **2006**, *8*, 1121-1125.

[2] D. A. Gomez-Gualdron, P. Z. Moghadam, J. T. Hupp, O. K. Farha, R. Q. Snurr, *J. Am. Chem. Soc.* **2015**, *138*, 215-224.

[3] G. M. Sheldrick, *Acta Crystallographica Section A: Foundations of Crystallography* **2008**, *64*, 112-122.

[4] A. C. Larson, R. B. Von Dreele, *Report LAUR 86-748. Los Alamos National Laboratory, NM* **1994**.

[5] A. L. Myers, J. M. Prausnitz, *AlChE J.* **1965**, *11*, 121-127.

[6] S. H. Hyun, R. P. Danner, *J. Chem. Eng. Data* **1982**, *27*, 196-200.

[7] E. D. Bloch, W. L. Queen, R. Krishna, J. M. Zadrozny, C. M. Brown, J. R. Long, *Science* **2012**, *335*, 1606-1610.

[8] S. Yang, A. J. Ramirez-Cuesta, R. Newby, V. Garcia-Sakai, P. Manuel, S. K. Callear, S. I. Campbell, C. C. Tang, M. Schroder, *Nat. Chem.* **2014**, *7*, 121-129.